ACS OMEGA

Open Access

http://pubs.acs.org/journal/acsodf

Article

Noninvasive Blood Pressure Monitoring via a Flexible and Wearable Piezoresistive Sensor

Bijender, Shubham Kumar, Amit Soni, Rimjhim Yadav, Surinder P. Singh, and Ashok Kumar*

Cite This: *ACS Omega* 2024, 9, 6355−6365

Read Online

ACCESS | Metrics & More | Article Recommendations | Supporting Information

ABSTRACT: In the present global context, continuous blood pressure (BP) monitoring is paramount in addressing the global mortality rates attributed to hypertension. Achieving precise insights into the human cardiovascular system necessitates accurate measurement of BP, and the accuracy depends on the faithful recording of oscillations or pulsations. This task ultimately depends on the caliber of the pressure sensor embedded in the BP device. In this context, we have fabricated a flexible resistive pressure sensor based on reduced graphene oxide (rGO) and a polydimethylsiloxane (PDMS) sponge that is highly flexible and sensitive. The designed device operates effectively with a minimal bias voltage of 500 mV, at which point it showed its maximum relative change in current, reaching approximately 25%. Additionally, the sensing device showed a notable change in resistance values, exhibiting almost 100% change in resistance when subjected to a pressure of 400 mmHg and high sensitivity of 0.27 $mmHg^{-1}$. After promising outcomes were obtained during static pressure measurement, the sensor was used for BP monitoring in humans. The sensor accurately traced the oscillometric waveform (OMW) for distinct systolic blood pressure (SBP) and diastolic blood pressure (DBP) combinations to cover a range of medical situations, including hypotension, standard or normal, and hypertension. The values of SBP, DBP, and MAP were derived from the sensor's output using the MAA technique, and the errors in these values concerning the simulator and the traditional BP monitor follow the universal AAMI/ESH/ISO protocols. Bland-Altman (B&A) correlation and scatter plots were used to compare the sensor's results and further validate the proposed sensor. The sensor showed the mean and standard deviation error in the SBP, DBP, and MBP of −0.2 ± 5.9, −0.5 ± 7, and −0.9 ± 4.7 mmHg when compared with the noninvasive blood pressure (NIBP) simulator. The pulse rate (PR) was also calculated from the same OMW for the specified value of 80 beats per minute (bpm) given by the simulator and reported a mean PR value of ∼81 bpm, close to the reference value. The findings show that the flexible resistive sensing device can accurately measure BP and replace the existing sensors of BP devices.

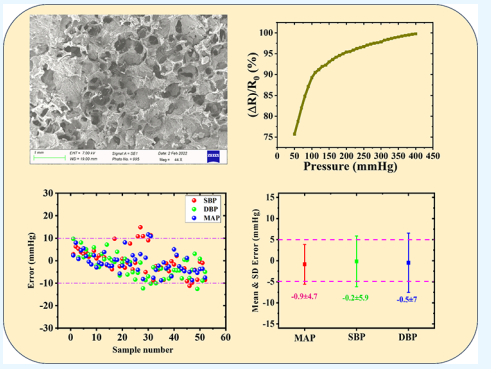

1. INTRODUCTION

BP is a dynamic physiological measure important in quantitatively identifying cardiovascular illnesses.[1,2] Cardiovascular illnesses are the most prevalent cause of death globally, contributing to around 18% of all fatalities.[3] Early diagnosis and continuous BP monitoring could stop many of these deaths. The primary reason for potentially fatal cardiovascular disorders such as cardiac arrest, coronary artery disease, and stroke is high BP, often known as hypertension[4] (also known as the "silent killer"). Over one-third of the population in India and around 1.13 billion people globally suffer from hypertension. Additionally, over 17 million fatalities per year worldwide occur due to hypertension.[5,6] The World Health Organization (WHO) has noted that hypertension prevention and control are vital to reducing death globally,[3] making it extremely important to monitor BP frequently for hypertension prognosis. Yet it is still challenging and highly desirable to monitor BP accurately by an arterial pulse to diagnose hypertension complications.

The pressure exerted on blood vessel walls by blood flow is called BP, and it can be measured using two techniques:[7−10] (1) Invasive and (2) Non-Invasive techniques. Out of these techniques, the noninvasive technique has gained widespread popularity due to its user-friendliness, eliminating the need for medical expertise and allowing individuals to utilize it conveniently at home. The noninvasive technique relies on oscillometry, tonometry, auscultatory, and photoplethysmography methods.[11−13] Since the last century, the auscultative process, which involves listening to the Korotkoff sound through a stethoscope, was formerly employed to assess BP.[14] However, in today's world, the oscillometry method is widely

Received: July 4, 2023
Revised: December 22, 2023
Accepted: January 18, 2024
Published: February 1, 2024

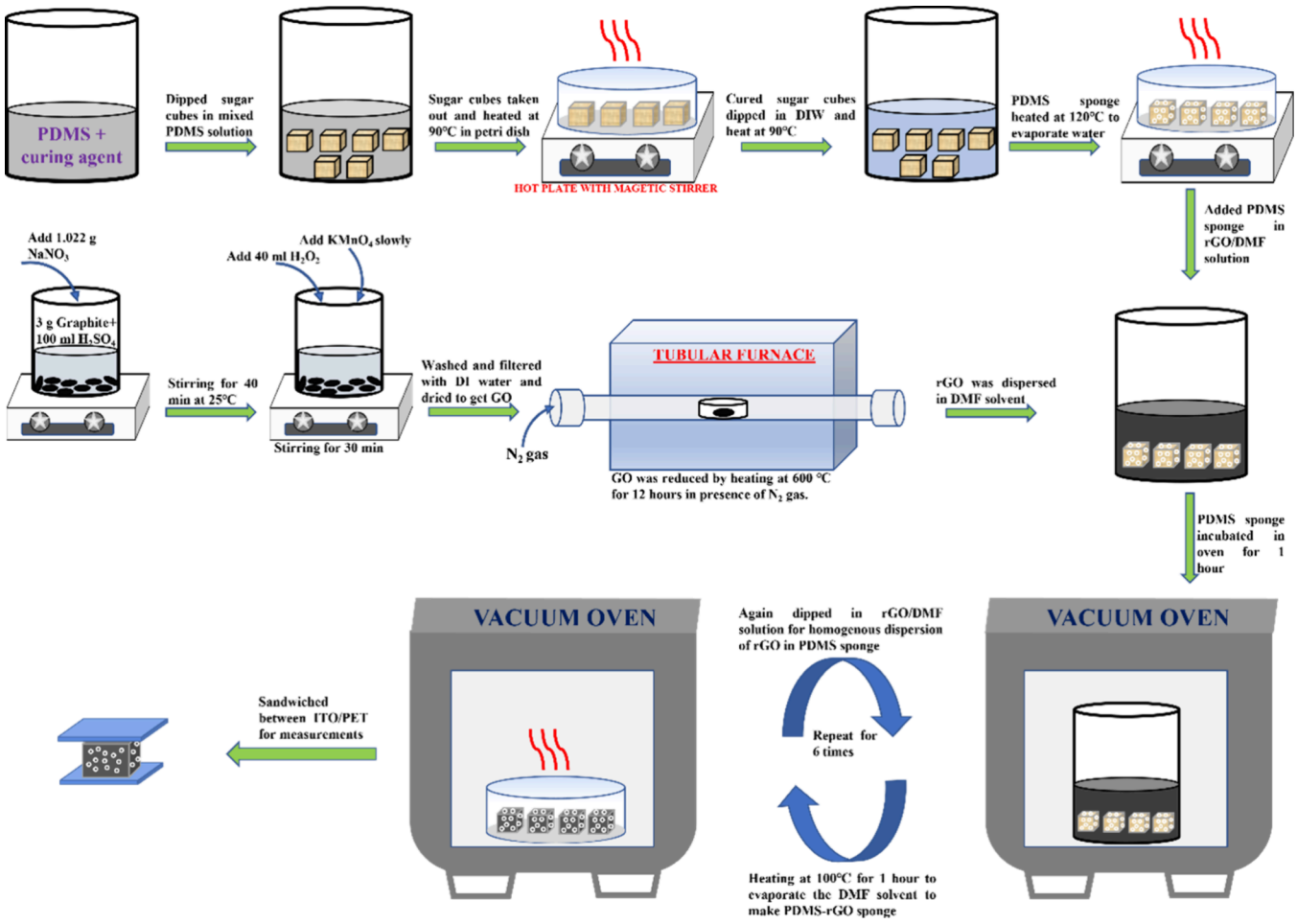

Figure 1. Schematic illustration of the fabrication process of the PDMS-rGO pressure sensor.

adopted because of its advantages, such as being simple to use, not requiring an expert, and providing BP readings automatically.[7,15]

In the oscillometric method, the SBP and DBP are calculated from the recorded oscillometric waveform envelope (OMWE), and this can be achieved through the utilization of various algorithms, including the maximum amplitude algorithm (MAA), linearizing the OMWE, zero crossing, and neural networks.[16,17] The most popular algorithm among them is MAA. In this, the SBP and DBP were determined using a predefined unique ratio of the maximum amplitude of the waveform (referred to as mean arterial pressure, or MAP).[18,19] In the present study, we also used the MAA to calculate the SBP and DBP values, and a range of specific ratios for systolic (from 0.45 to 0.60) and diastolic (from 0.65 to 0.80) was taken as provided in the literature.[20,21]

Numerous automated BP monitoring devices on the market use the oscillometry approach, but one of the most significant challenges they face is the accuracy of the measured BP values. The primary causes of the error in these automated devices are the oscillations recorded in OMWE and the algorithm used to calculate the BP. The algorithm employed in BP monitors is protected as a trade secret and never made accessible to the public. Thus, to get a precise BP measurement, oscillations or pulsations must be recorded accurately, which entirely depends on the quality of the pressure sensor used in BP devices. Hence, a highly sensitive pressure sensor with excellent performance is required in the BP measurement.

Flexible and wearable pressure sensors are crucial in numerous applications, including artificial intelligence,[22−24] monitoring human health,[25−28] medical diagnosis,[29−32] and man-machine interface.[33−35] They are easily attached to the human body due to high flexibility and collect data from the human body correctly and efficiently to provide complete information about the cardiovascular system, including BP, PR, and information on physiological movements.[36] Every pressure sensor works with a different sensing method and typically functions as a transducer to transform applied pressure into an electrical signal. They are classified into four types based on the sensing mechanism: capacitive,[37−41] piezo-resistive,[42−47] piezo-electric,[48−50] and triboelectric[51−53] pressure sensors. Due to their straightforward design, high sensitivity, rapid response, high precision, and long -life, piezoresistive sensors have attracted the most interest among them.[24,54−56] These sensors record the variations in resistance value resulting from applying external pressure. Due to high sensitivity and quick response characteristics, they are more suited for biological applications in medical detection equipment. Many researchers reported the piezoresistive sensing devices, mainly conducting materials or nanowires,[57−60] and explored their applications in wearable devices,[54,61−63] robotic skin,[64,65] and electronic skin.[66−68]

To meet the demand for a highly sensitive pressure sensor with a quick response in BP measurement devices, we have developed a piezoresistive sensor by using a PDMS sponge as an elastic material and rGO as a conductive material. The

https://doi.org/10.1021/acsomega.3c04786
ACS Omega 2024, 9, 6355−6365

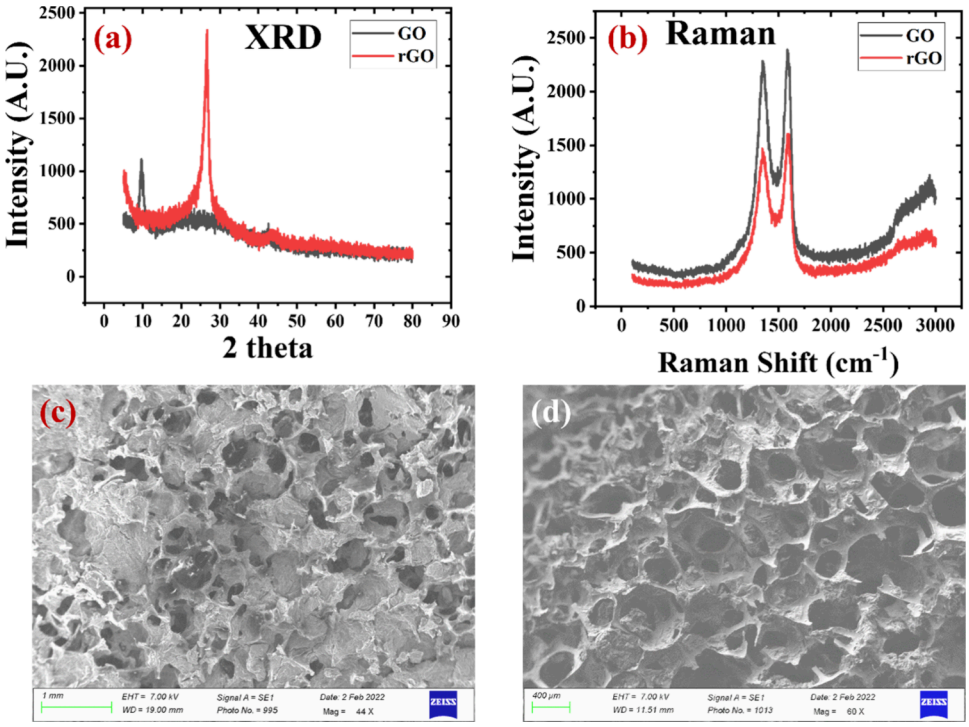

Figure 2. (a, b) XRD and Raman analysis to confirm the formation of GO and rGO. (c, d) Top and side view SEM images of the developed sponge PDMS-rGO layer.

PDMS sponge or foam was used due to its many advantages, as reported by the researchers.[69,70] The proposed sensor performs well while measuring static pressure and requires a very low operating voltage. After great results were achieved, the sensor was utilized for BP measurement. The sensor was tested for 52 predefined oscillometric waveforms using the (NIBP) simulator. The SBP, DBP, and MAP values were calculated using a Python program based on the MAA. The sensor's accuracy was investigated by comparing the computed BP values obtained with the NIBP analyzer and the BP device. The designed sensor exhibited a minor deviation in the SBP, DBP, and MAP values, which are under international protocols set out by the American Association for the Advancement of Medical Instrumentation, the European Society of Hypertension, and the International Organization for Standardization (AAMI/ESH/ISO) standards,[71] which are necessary for BP measurement appliances. Additionally, by utilizing the same algorithm, the PR was extracted from the OMWE because monitoring PR is significant in the domains of healthcare and biomedical engineering and is necessary for determining a person's physiological status.

2. EXPERIMENTAL METHODS

2.1. Preparation of the Sponge PDMS Layer. As a template for forming the sponge PDMS layer, sugar cubes of side length 20 mm purchased locally were used. As illustrated in Figure 1, PDMS prepolymer and its curing agent (Dow Corning, Sylgard 184) were mixed in a weight ratio of 10:1 in a beaker with the help of a magnetic stirrer. The mixed solution is treated in the vacuum-desiccated oven to eliminate any unintentionally trapped air bubbles. After that, sugar cubes were dipped in the solution for 30 min at room temperature. Through capillary action, the PDMS solution penetrated the space of the sugar cube template. The loaded sugar cubes with PDMS were taken out and heated on a hot plate for 1 h in a Petri dish at 90 °C to cure them. The cured PDMS-filled sugar cubes were dipped into deionized water (DIW) and heated to 90 °C for 30 min. Before this, a tiny layer from one face of the cubes was trimmed to prevent a hindrance during the sugar's breakdown. The process was repeated three times to dissolve the sugar template completely in the DIW and obtain pure PDMS foam. After complete dissolution, the PDMS sponge was heated at 120 °C for 30 min to evaporate the residual water and a thoroughly dried PDMS sponge was obtained.

2.2. Formation of Reduced Graphene Oxide (rGO). A modified version of Hummer's approach was adopted to create graphene oxide chemically.[72,73] Natural graphite with a mesh size of 500 nm was used in this procedure as a basic reaction precursor. As shown in Figure 1, 3 g of graphite was dissolved in 1.022 g of $NaNO_3$ and 100 mL of H_2SO_4 solution, and the mixture was vigorously shaken for 40 min at 25 °C. $KMnO_4$ was then gradually added to the solution and stirred once more for 40 min at 25 °C, resulting in a slow, controlled oxidation reaction. The mixture was then diluted with 250 mL of DIW before 40 mL of H_2O_2 was added. As a result of the rapid rate of oxidation reaction and significant surface defect observed in the acidic aqueous medium, an additional 500 mL of DIW was added to the solution to dilute it further. Additionally, after adding H_2O_2, the oxidation was quenched, and the subsequent process was stopped. The solution was washed and filtered 6−7 times using DIW to remove unreacted ions and contaminants. Then, to remove all of the moisture, GO flakes are dried at ambient temperature and finally stored in a vacuum desiccator to avoid humidity. Raman studies and XRD results verified that GO was formed. GO was reduced by heating in a tube furnace at 600 °C for 12 h in the presence of N_2 gas. The formation of rGO was also confirmed by XRD and Raman Analysis.

2.3. Formation of the Sponge PDMS-rGO Layer. The fabricated rGO was dispersed in 100 mL of *N*,*N*-

https://doi.org/10.1021/acsomega.3c04786
ACS Omega 2024, 9, 6355−6365

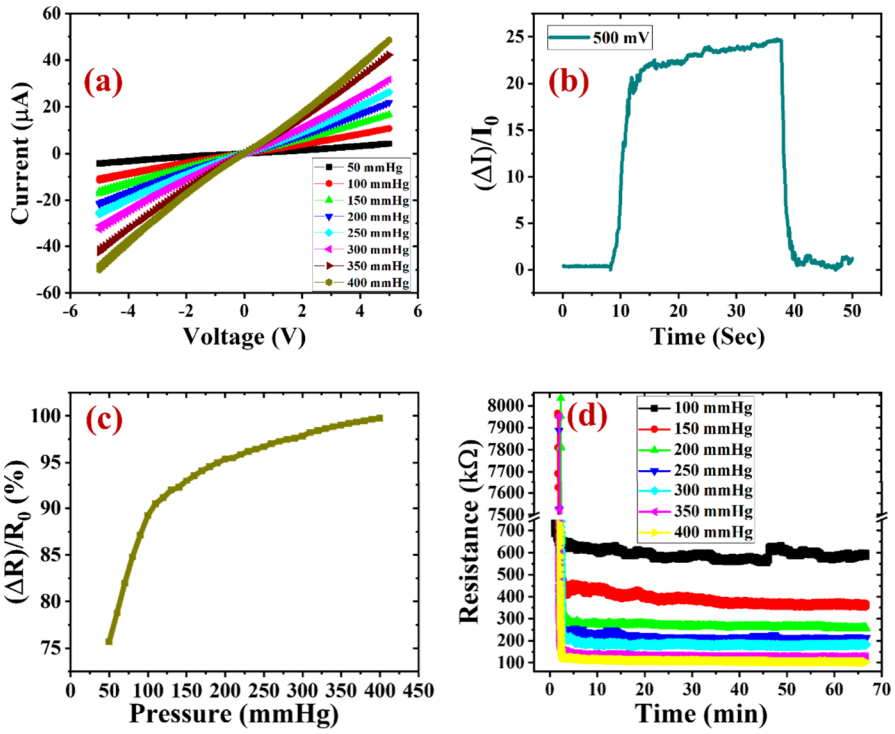

Figure 3. Performance of the developed pressure sensor under static pressure measurement. (a) $I-V$ characteristics at various applied pressures from 50 to 400 mmHg. (b) Relative change in current at a bias voltage of 500 mV. (c) Output response curve of the fabricated sensor regarding the relative change in resistance with applied pressure ranges from 50 to 400 mmHg. (d) Sensor's working stability test under the external pressure of 100 to 400 mmHg with a gap of 50 mmHg.

dimethylformamide (DMF) with the help of a homogenizer. The solution was sonicated for 2 h for a homogeneous mixture of rGO and DMF. The developed PDMS sponges were dipped into the solution and incubated in a vacuum oven for 1 h. After 1 h, the dipped PDMS sponge was taken out and heated at 100 °C for 1 h to evaporate the DMF present in it. The dipping process followed by heating was repeated six times to produce a uniform distribution of the rGO with the PDMS network.

2.4. Fabrication of the PDMS-rGO Foam Sensor. The indium tin oxide (ITO)-coated poly(ethylene terephthalate) (PET) substrate performed the role of the electrode. As demonstrated in Figure 1, the produced PDMS-rGO sponge layer was inserted between the ITO/PET substrates, with the adhesive layer between them being provided by silver paint. Before incorporation, a thin layer of silver paint was applied to the ITO/PET surface and heated to 100 °C for robust adherence. The electrical connections were made using copper for further measurement of the developed sensor.

2.5. Pressure Sensor Characterization and Measurements. XRD and Raman's studies were used to confirm the synthesis of GO and rGO. Scanning electron microscopy (SEM) was used to determine the microstructuring or existence of porosity inside the PDMS-rGO layer. The sensor's performance for static pressure and the BP measurement was tested using a source meter (Keithley 2400), mandrel (an artificial human hand), and NIBP simulator. The fabricated sensor was fastened to the mandrel, and a cuff was wrapped over it. The NIBP simulator was used to apply pressure to the cuff. It also provided various BP values for assessment.

3. RESULTS AND DISCUSSION

3.1. Fabrication Process and Structural Analysis. The proposed sensor was fabricated by using a sponge PDMS layer and rGO as a conductive material. The sponge PDMS layer was developed using a sugar cube as a template, and rGO was made from graphite, as illustrated in Figure 1.

According to Figure 2a,b, the XRD and Raman studies supported the production of GO and rGO. In XRD analysis, the sharp peak for GO was observed at 2θ of 9.52°, indicating complete oxidation of the graphite into GO. However, in rGO, the sharp peak shifted to 26.46°, proving that the oxygen-containing functional groups were largely reduced during the reduction process, as shown in Figure 2a. The D and G vibration bands for GO were found at 1348.52 and 1594.81 cm^{-1} in the Raman analysis, which further confirmed how well graphite was converted into GO. The D and G vibration bands for rGO were observed at 1353.78 and 1586.67 cm^{-1}, as shown in Figure 2b, which claims that the GO was well reduced, and the oxygen functional groups were eliminated. The SEM images illustrate the presence of the large pores inside the PDMS-rGO layer and show that the rGO was well distributed and connected with the PDMS network of the sponge layer, as shown in Figure 2c,d.

3.2. Sensor's Performance under Static Pressure Measurement. The fabricated sensor was attached to the mandrel for the static pressure measurement, and a cuff was wrapped over it. The cuff was attached to the NIBP simulator, which is used to apply the static pressure of different values. The sensor's response was evaluated using a Keithley 2400 current−voltage source meter. First, it was determined how the sensor's current (I) versus voltage (V) characteristics varied with the applied static pressure. It was found that the slope of

https://doi.org/10.1021/acsomega.3c04786
ACS Omega 2024, 9, 6355−6365

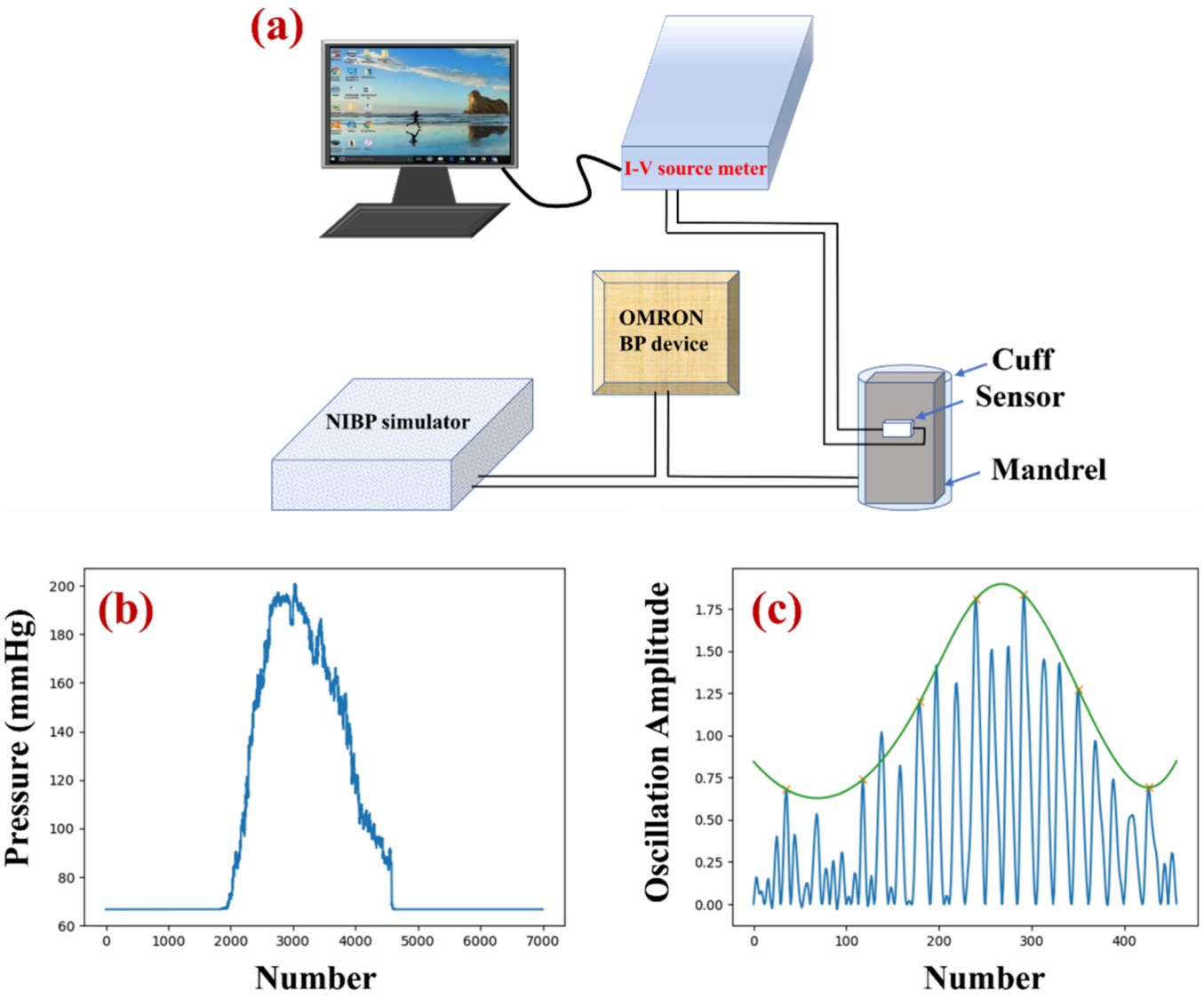

Figure 4. BP measurement using the developed sensor. (a) Schematic diagram of the experimental setup for the measurement. (b) Output signal of the sensor during the BP measurement. (c) Extracted oscillometric waveform with envelope.

the $I-V$ curve increased with the applied pressure, ranging from 50 to 400 mmHg, as shown in Figure 3a. The increased applied pressure significantly decreased the sensor's resistance. Figure S1 shows a detailed study of the current variation with voltage at different applied pressure values. This indicates that the sensor's resistance decreased when the applied pressure increased.

Power consumption is a crucial factor in the performance of any resistive sensing device. As a result, we also determined the lowest bias voltage needed for the designed sensor to be operational. At a constantly applied pressure of 200 mmHg, the relative fluctuations in the current $(\Delta I/I_0)$ were recorded with varied voltage from 50 mV to 10 V. At start, the change in the current value increased as the applied voltage increased from 50 mV to 500 mV, as shown in Figure S2(a and b), but then decreased from 500 mV to 10 V. As shown in Figure 3b, the most dramatic change in current was observed for an applied voltage of 500 mV, indicating that the developed sensor requires a very low bias voltage of 500 mV. All the experiments were carried out at a bias voltage of 500 mV, as discussed in the following paragraph.

After that, the relative difference in the resistance value $(\Delta R/R_0)$ was measured by applying the pressure from 50 to 400 mmHg with a gap of 20 mmHg. The change in the resistance was approximately 75% for the applied pressure of 50 mmHg was increased with the increase in external pressure. At the maximum external pressure of 400 mmHg, the sensor showed a 100% variation in its resistance value, as demonstrated in Figure S3. The variation in the resistance value $(\Delta R/R_0)$ of the proposed sensing device with the full range of external pressure is shown in Figure 3c. The sensor showed a linear behavior in different applied ranges, and by using the response curve, the sensitivity of the developed sensor $(S = \delta(\Delta R/R_0)/\delta P)$ was calculated in different pressure regions, as represented in Figure S4. The sensing device exhibited a high sensitivity (%) of 0.27 $mmHg^{-1}$ for the applied pressure region of 50 to 100 mmHg, as given in Figure S4a. The operational stability, one of the important factors in checking the performance of the sensing device, was investigated during static pressure measurements. Seven different applied pressure values were used to test the functioning stability, and the sensor showed a constant change

https://doi.org/10.1021/acsomega.3c04786
ACS Omega 2024, 9, 6355−6365

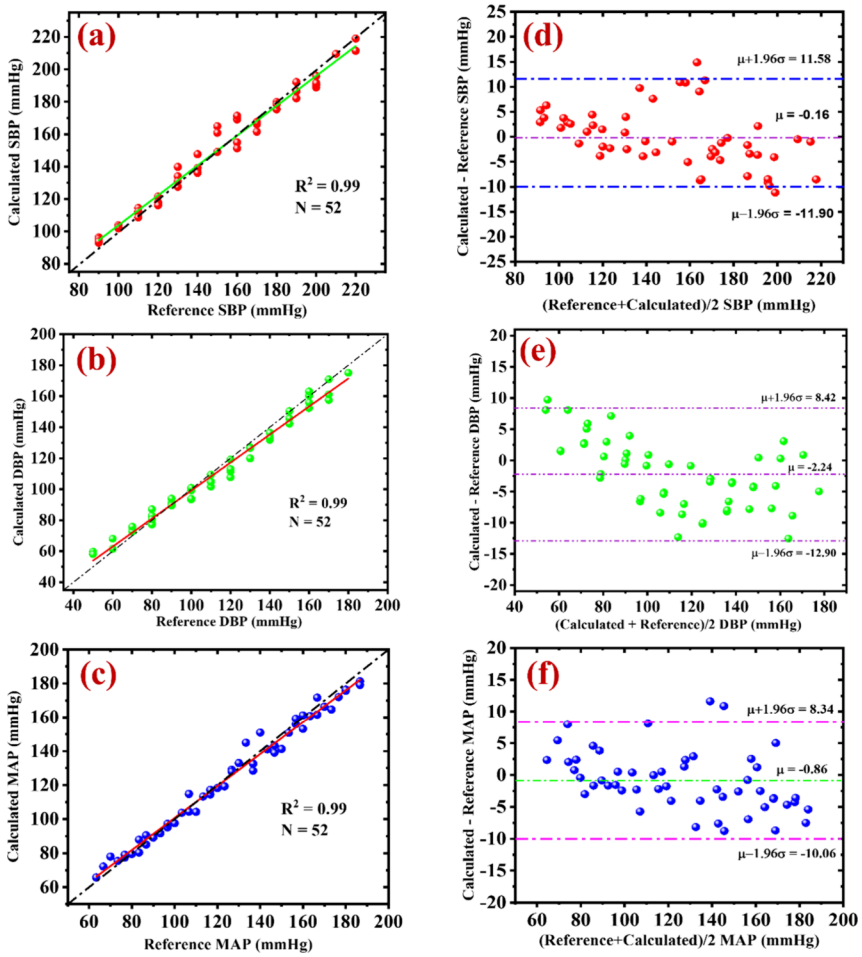

Figure 5. Comparison of the sensor's SBP, DBP, and MAP values with the reference values (simulator). (a−c) Correlation plots with the N (number of samples) and Pearson coefficient (R^2). (d−f) B&A plots, in which the dash-dotted line denotes the mean differences μ and 95% criteria of agreement ($\mu \pm 1.96\sigma$).

in the resistance value for roughly 70 min at each pressure value, as illustrated in Figure 3d. Thus, the fabricated sensor has high sensitivity, good operational stability, and an extensive operating pressure range and only requires a low bias voltage, making it suitable for monitoring human BP.

3.3. Sensor's Application in Monitoring Human Blood Pressure (BP). *3.3.1. Data Collection and Processing.* As described in the schematic diagram of the experimental setup (as shown in Figure 4a) for the BP and PR measurement, the developed sensor was attached to the mandrel. A cuff was wrapped over it, as we have done the same for static pressure measurement: the NIBP simulator and a commercial BP measurement device (OMRON HEM-7130) connected to the cuff. The sensor's response in terms of resistance was recorded using an $I-V$ source meter. The BP device was utilized to apply pressure to the cuff during measurement and for comparison with computed BP values from the proposed sensor. The NIBP simulator was used to configure the BP values with various SBP and DBP given to the sensor. The 52 distinct BP values/conditions were generated using the NIBP simulator to represent the different health conditions like hypotensive, normal, and hypertensive BP states (Table S1). For these 52 distinct combinations, the SBP values were set between 90 and 220 mmHg and the DBP values were between 50 and 180 mmHg. The simulator automatically provides the MAP value; however, the BP device does not provide the MAP value. A facile formula MAP = 1/3 (SBP) + 2/3 (DBP) was used to calculate MAP for the BP device. The PR value was fixed for each BP measurement at 80 bpm.

During the measurement, the BP monitor applies pressure to the cuff and increases the pressure in the pneumatic system to a maximum value greater than the set SBP value (as determined by the simulator). After reaching its maximum pressure, the cuff reduced the pressure at a 3−4 mmHg/s rate. While doing so, the simulator detects the pneumatic pressure inside the cuff and produces pulses following the preset SBP and DBP values. The sensor's output response during the inflation and deflation was recorded, as illustrated in Figure 4b, and processed to determine the SBP, DBP, MAP, and PR values.

We must process the data collected from the sensor's output signal to compute the BP values. A Python-based program (give the details/name) using the MAA approach was built for data processing. This approach began by uploading the sensor's output signal into the software and then collecting its deflation curve. The collected deflation curve (as illustrated in Figure 4b) comprised two parts: the first was the pressure in the cuff that the BP device gradually applied, and the second, the pressure pulsation, commonly referred to as oscillometric pulses, that were produced by the NIBP simulator. The oscillometric pulses associated with the deflating curve were extracted by fitting the second-order polynomial, which

https://doi.org/10.1021/acsomega.3c04786
ACS Omega 2024, 9, 6355−6365

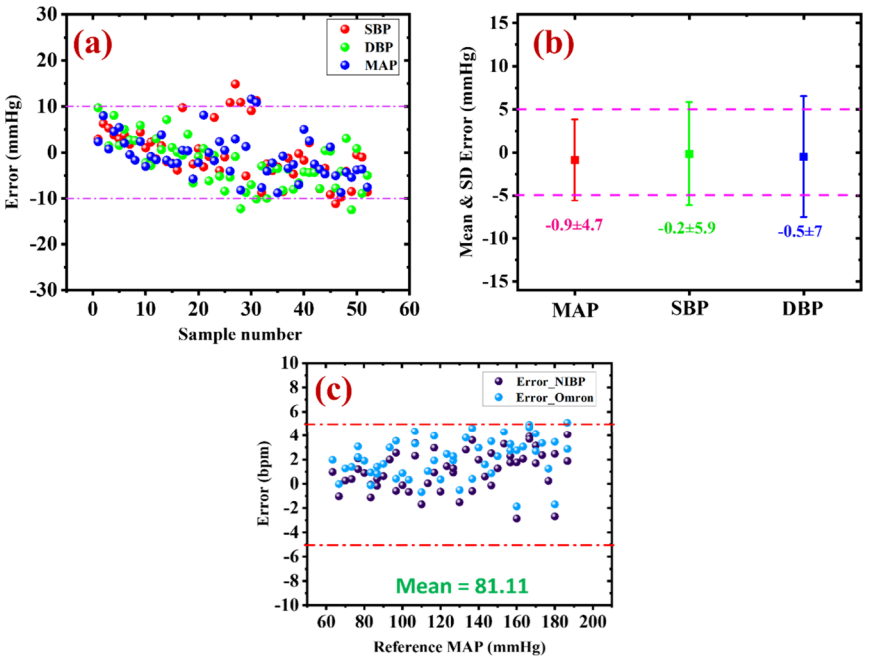

Figure 6. To validate the sensor's results as per the AAMI/ESH/ISO universal standards. (a) B&A plot for BP values in relation to the simulator, the dashed-dotted line illustrates the error limit of 10 mmHg. (b) Mean and standard deviation of the error between the results from the sensor and the simulator, the dashed line shows the maximum allowable mean error of 5 mmHg by protocols. (c) Error in the sensor's reading of the human pulse concerning the NIBP analyzer and the OMRON BP device.

provided the best-fit curve. All of the extracted oscillometric pulses form a waveform called the OMW. The Savitzky−Golay filter was used to smooth the data after obtaining the OMW, and a zero baseline was generated by picking the lowest peaks to figure out the real height of every pulse. The cubic spline interpolation was used to generate the upper envelope and afterward smoothed by the adjacent-averaging technique.[74]

3.3.2. Computation of BP and PR Values. The SBP and DBP values can be computed from OMWE using various characteristic ratios. The systolic coefficient can range from 0.45 to 0.73 in multiple devices, while the diastolic coefficient can range from 0.69 to 0.83.[7,75] In the present investigation, 52 different human BP conditions were performed, and their corresponding OMWEs were collected by utilizing the developed pressure sensor. A range of characteristic ratios for SBP and DBP, i.e., for SBP from 0.45 to 0.65 and DBP from 0.60 to 0.80, were taken to compute the BP values from the obtained OMWEs. The range of characteristic ratios was chosen to determine which ratio for SBP and DBP would produce the BP results with the lowest errors. A thorough analysis was conducted using the SBP and DBP characteristic ratio ranges for all 52 situations. The ratio of every systolic and diastolic characteristic with its error and the standard deviation is shown in Figure S5. The error with standard deviation was found to be the least for the systolic ratio of 0.56 and diastolic ratio of 0.70. Thus, we proceed further with these ratios to compare the computed BP values and the reference BP values taken from the simulator and BP device. The MAP value was obtained for the developed sensor from the maximum amplitude of OMWE and the BP device and simulator, and it was calculated from the formula, i.e., MAP = 1/3 (SBP) + 2/3 (DBP). For example, for the 120/80 mmHg value given by the simulator, the computed SBP and DBP values at various ratios are shown in Table ST2. The SBP and DBP were 118 and 80 mmHg for the above-optimized ratios, respectively. The BP device's SBP and DBP values were 126 and 80 mmHg. The MAP values for the simulator, BP device, and developed sensor were 93.33, 95.33, and 91.67, respectively. The deviation in the measurement of BP was identified by deducting the actual (or reference) BP from the computed values. Thus, for the set value of 120/80 mmHg, the SBP, DBP, and MAP inaccuracy was −1.97, 0.62, and −1.66 mmHg compared to the simulator. Here, the SBP and MAP were marginally underestimated, respectively (negative error), while the DBP was somewhat overestimated (positive error). In this way, the BP values were calculated for the remaining 52 BP situations and the corresponding errors were also determined in relation to the simulator value (the reference value).

This study also measured the pulse rate for the same 52 BP configurations. The PR was calculated by estimating the pulses (n) that occurred between the first and last troughs of the OMW. The given PR value remained unchanged during the entire BP measurement, which was 80 bpm. The PR values from the sensor's output were acquired from the OMW using the same software as we did for BP evaluations, and the associated errors were also determined concerning the simulator and BP device value. The obtained mean value of PR was 81.11 bpm.

3.3.3. Analysis of Error in BP and PR. As demonstrated in Figure 5a−c, a correlation plot was used to compare the calculated SBP, DBP, and MAP values with the corresponding reference BP of the simulator. For all parameters (i.e., SBP, DBP, and MAP), Pearson's correlation coefficient (R) was more than or equal to 0.97, indicating a significant relationship between the computed and actual BP. The developed sensing device exceeds SBP and DBP in the low BP region to some extent but is underestimated in the high BP range, as shown in Figure 5a,b. Like MAP, the sensor overestimated low BP ranges and somewhat underestimated high BP ranges, as shown in Figure 5c.

https://doi.org/10.1021/acsomega.3c04786
ACS Omega 2024, 9, 6355−6365

The error was then further evaluated using B&A analysis.[76] The primary purpose of this method is to illustrate the conformity between two quantitative measures by presenting the variation between derived and actual values versus the mean of both values. Figure 5d−f displays the B&A scatter plot for SBP, DBP, and MAP, along with mean bias and the 95% limit of agreement. The range that 95% of the total divergence points are predicted to fall inside is known as the limit of agreement. The tiny inaccuracy in the graph suggests that the two methods agree pretty well. When the data for each BP measurement were independently examined, the mean differences (μ) for SBP, DBP, and MAP were 0.16, 2.24, and 0.86 mmHg, respectively, with standard deviations (σ) of 5.9, 5.4, and 4.7 mmHg (shown in Figure 5d−f). Therefore, the variations in BP readings fall inside the confidence interval.

In the last few decades, several organizations, such as AAMI, ESH working on BP monitoring, and the ISO, have developed protocols for clinical validation of BP measuring devices. However, it is acknowledged that patients, consumers, and manufacturers would be best served if all BP measurement instruments were evaluated for accuracy by a single universally accepted validation process. As a result, the AAMI, ESH, and ISO experts took an international initiative to establish a global standard for device validation that has now superseded all of the earlier protocols and standards. As per the AAMI/ESH/ISO protocol, the reliability of a BP instrument is expressed in terms of (i) the threshold probability of acceptable inaccuracy or error and (ii) the mean error (also known as average error) along with its standard deviation. For noninvasive BP measurement equipment, these protocols should be followed for the device to be widely accepted and highly accurate. Under this protocol, equipment must meet the following conditions to pass the criteria: (i) the error must be lower than 10 mmHg in 85% or more of the measurement, and (ii) the total measurement inaccuracy must be below 5 mmHg in mean and 8 mmHg in standard deviation.[71] The BP values within 5, 10, and 15 mmHg error and typical Bland-Altman (B&A) scatter plots must be presented.

In this context, we presented the BP variation in SBP, DBP, and MAP compared to the analyzer with a 10 mmHg error limit. As shown in Figure 6a, 90.4% of SBP values, 96.2% of DBP values, and 96.2% of MAP values are within the 10 mmHg range. The average and standard deviation error in BP values were also computed for the second protocol condition. As demonstrated in Figure 6b, the values for SBP, DBP, and MBP were -0.2 ± 5.9, -0.5 ± 7, and -0.9 ± 4.7 mmHg, respectively.

The PR values were also determined using the same software as mentioned before from the output of the designed sensor. The simulator provided a PR value of 80 bpm; the error in the derived PR concerning the simulator and BP device (provided by it) was also evaluated and is displayed in Figure 6c. Compared to a simulator and a BP device (OMRON), the PR values' inaccuracy was within 5 bpm. The average PR value from the sensor was 81.11, displaying a substantial connection between the standard and evaluated data.

Meanwhile, the designed sensor and the BP device used identical OMW produced by the analyzer to determine the BP. Consequently, it is imperative to analyze the sensor's accuracy using BP equipment. Even though there are numerous BP monitors on the market, they are doubtful of fulfilling the criteria of the AAMI/ESH/ISO standards. Regarding this, we initially validated the BP device by utilizing the NIBP analyzer, and then, the sensor outcomes were compared to it. In this respect, the values from the BP device and the simulator were compared.

First, the correlation plot was used to compare the SBP and DBP values of the BP device (OMRON) with the standard BP values of the simulator, as demonstrated in Figure S6a,b. This was similar to what we did for the sensor and the simulator. As can be seen from the figures, R has a value of 0.99, while the BP device consistently overestimated the SBP for all reference BP values. Still, it did a great job of estimating the DBP, which means it accurately estimated the DBP. In the B&A plot, as represented in Figure S6c,d, the mean differences (μ) for SBP and DBP were 5.62 and 0.52 mmHg, respectively, with standard deviations (σ) of 0.6 and 1.3 mmHg. Therefore, 95% of the total variation points fall inside the confidence interval. The average error and standard deviation for SBP and DBP were also calculated to check the AAMI/ESH/ISO protocol requirement. Figure S6e shows the average error and standard deviation for the BP device with the simulator, and their values for SBP, DBP, and MAP were 5.6 ± 0.6, -0.5 ± 1.3, and 1.5 ± 0.8 mmHg, respectively. As a result, the average or mean and standard deviation errors for the commercial BP device relative to the simulator precisely match the validation protocols and allow for a comparison of the computed results with the BP device.

Figure S7 compares the computed findings of the designed sensor and the commercial BP device using correlations and B&A plots. For SBP and MAP, the Pearson coefficient was 0.99, indicating a significant correlation with the BP device. The 95% confidence interval also encompasses more than 95% of the various SBP, DBP, and MAP data points. The scatter plot and average and standard deviation error plot, in accordance with the protocols, are presented in Figure S8. From the scatter plot, we can determine that more than 95% of the SBP, DBP, and MAP measurements are within the permissible error range of 10 mmHg. On the other hand, the average and standard deviation error for SBP, DBP, and MAP in relation to the BP device was -3.7 ± 6.0, 0.02 ± 6.2, and -2.4 ± 4.6 mmHg, respectively (Figure S8b). According to the findings, the developed device is precise when tested on the NIBP analyzer and the BP device.

The developed sensors met all of the standard protocols for laboratory-level test measurement requirements and displayed outstanding performance in the BP measurement. Overall, the results show that our developed sensor accurately measures human BP and can be used as a wearable device to track both BP and other physiological activities.

4. CONCLUSIONS

In this research, we developed a highly sensitive and flexible resistive pressure sensor by using a PDMS-rGO sponge layer. We created the PDMS-rGO sponge layer using a sugar cube technique, while the rGO was made by reducing self-produced GO. After carefully calibrating its pressure-dependent properties, we applied the sensor to monitor human BP and PR. The operating voltage of the developed sensor was determined by applying different bias voltages, and it was found that the sensor works well with a very low bias voltage of 500 mV. In static pressure measurements, the sensor proved stable and responsive, showing a significant change in resistance, close to 100%, when subjected to a pressure of 400 mmHg. This responsiveness translated to a high sensitivity level of 0.27 $mmHg^{-1}$. With these promising results from static pressure

https://doi.org/10.1021/acsomega.3c04786
ACS Omega 2024, 9, 6355−6365

measurements, the sensor was used for human BP monitoring. During the BP measurement phase, the sensor followed the oscillometric waveform for all 52 predetermined conditions set by an NIBP simulator. The SBP, DBP, and MAP values were calculated from the traced OMW using a Python program based on the MAA. The computed BP values obtained from the sensor were compared with both the simulator and the conventional BP device with the help of correlation, B&A, and scatter plots. The outcome of this comparison indicated that the values garnered from the sensor and those obtained from the conventional BP device exhibited interchangeability. The mean error and standard deviation for SBP, DBP, and MAP were within the established global guidelines stipulated by the standard AAMI/ESH/ISO protocols. Furthermore, PR was calculated for a specified value of 80 beats per minute (bpm) as provided by the simulator. Remarkably, the sensor reported an average PR value of 81.11 bpm, closely aligning with the reference value. As a result, the developed sensor accurately assessed the BP and PR with a tolerable error across diverse combinations of SBP and DBP values reflective of various health conditions. Therefore, due to its remarkable performance in BP monitoring, this proposed sensor holds the potential to replace existing pressure sensors utilized in conventional BP devices, offering improved accuracy and reliability. Importantly, this work introduces a unique approach, as using such a flexible resistive sensor for BP monitoring via the oscillometry method has not been previously documented. Moreover, due to its high flexibility owing to the sponge layer, the sensor's scope extends to the monitoring of various physiological activities. Its spatial adaptability makes it suitable for applications like robotics and electronic skin.

■ ASSOCIATED CONTENT

Supporting Information

The Supporting Information is available free of charge at https://pubs.acs.org/doi/10.1021/acsomega.3c04786.

> Current−voltage changes with different pressures and the current at different bias voltages; Change of resistance of the sensor for the complete applied pressure ranging from 50 to 400 mmHg and sensitivity of the sensor in defined different applied pressure ranges; mean and standard deviation error for the systolic and diastolic characteristics ratios and compares the sensor's results (SBP, DBP, and MAP) with the traditional BP device using correlation, Bland-Altman, and scatter plots; table also shows SBP and DBP values for a certain characteristic ratio of 120−80, which helps us understand how BP values change with these ratios (PDF)

■ AUTHOR INFORMATION

Corresponding Author

Ashok Kumar − *CSIR-National Physical Laboratory, New Delhi 110012, India; Academy of Scientific and Innovative Research (AcSIR), Ghaziabad 201002, India;* orcid.org/0000-0001-9283-4122; Email: ashok553@nplindia.org

Authors

Bijender − *CSIR-National Physical Laboratory, New Delhi 110012, India; Academy of Scientific and Innovative Research (AcSIR), Ghaziabad 201002, India;* orcid.org/0000-0002-5104-7170

Shubham Kumar − *CSIR-National Physical Laboratory, New Delhi 110012, India; Academy of Scientific and Innovative Research (AcSIR), Ghaziabad 201002, India;* orcid.org/0000-0002-5185-890X

Amit Soni − *CSIR-National Physical Laboratory, New Delhi 110012, India; Academy of Scientific and Innovative Research (AcSIR), Ghaziabad 201002, India*

Rimjhim Yadav − *CSIR-National Physical Laboratory, New Delhi 110012, India; Academy of Scientific and Innovative Research (AcSIR), Ghaziabad 201002, India*

Surinder P. Singh − *CSIR-National Physical Laboratory, New Delhi 110012, India; Academy of Scientific and Innovative Research (AcSIR), Ghaziabad 201002, India*

Complete contact information is available at: https://pubs.acs.org/10.1021/acsomega.3c04786

Notes

The authors declare no competing financial interest.

■ ACKNOWLEDGMENTS

The authors thank the Director, CSIR-NPL, and Head, the Physico-Mechanical Metrology division, CSIR-NPL, for their support and constant encouragement. Mr. Bijender wants to thank Pallvi Dariyal and Sony Bharadwaj for their help and support. Mr. Bijender also wants to thank AcSIR and CSIR-NPL for pursuing the Ph.D. program.

■ REFERENCES

(1) Luo, N.; Dai, W.; Li, C.; Zhou, Z.; Lu, L.; Poon, C. C. Y.; Chen, S. C.; Zhang, Y.; Zhao, N. Flexible Piezoresistive Sensor Patch Enabling Ultralow Power Cuffless Blood Pressure Measurement. *Adv. Funct Mater.* **2016**, *26* (8), 1178−1187.

(2) Kannel, W. B. Blood Pressure as a Cardiovascular Risk Factor: Prevention and Treatment. *JAMA* **1996**, *275* (20), 1571−1576.

(3) Panula, T.; Koivisto, T.; Pänkäälä, M.; Niiranen, T.; Kantola, I.; Kaisti, M. An Instrument for Measuring Blood Pressure and Assessing Cardiovascular Health from the Fingertip. *Biosens Bioelectron* **2020**, *167*, No. 112483.

(4) Chobanian, A. V.; Bakris, G. L.; Black, H. R.; Cushman, W. C.; Green, L. A.; Izzo, J. L.; Jones, D. W.; Materson, B. J.; Oparil, S.; Wright, J. T.; Roccella, E. J. Seventh Report of the Joint National Committee on Prevention, Detection, Evaluation, and Treatment of High Blood Pressure. *Hypertension* **2003**, *42* (6), 1206−1252.

(5) Anchala, R.; Kannuri, N. K.; Pant, H.; Khan, H.; Franco, O. H.; Di Angelantonio, E.; Prabhakaran, D. Hypertension in India: A Systematic Review and Meta-Analysis of Prevalence, Awareness, and Control of Hypertension. *J. Hypertens* **2014**, *32* (6), 1170.

(6) Ke, C.; Gupta, R.; Shah, B. R.; Stukel, T. A.; Xavier, D.; Jha, P. Association of Hypertension and Diabetes with Ischemic Heart Disease and Stroke Mortality in India: The Million Death Study. *Glob Heart* **2021**, *16* (1), 69.

(7) Forouzanfar, M.; Dajani, H. R.; Groza, V. Z.; Bolic, M.; Rajan, S.; Batkin, I. Oscillometric Blood Pressure Estimation: Past, Present, and Future. *IEEE Rev. Biomed Eng.* **2015**, *8*, 44−63.

(8) Lehman, L. W. H.; Saeed, M.; Talmor, D.; Mark, R.; Malhotra, A. Methods of Blood Pressure Measurement in the ICU. *Crit Care Med.* **2013**, *41* (1), 34.

(9) Jazbinsek, V.; Luznik, J. EMBEC'05, Z. T.-I. proceedings of; 2005, undefined. *Non-Invasive Blood Pressure Measurements: Separation of the Arterial Pressure Oscillometric Waveform from the Deflation Using Digital Filtering*. 2005; Vol. *11*(1).

(10) Kumar, R.; Dubey, P. K.; Zafer, A.; Kumar, A.; Yadav, S. Past, Present and Future of Blood Pressure Measuring Instruments and Their Calibration. *Measurement* **2021**, *172*, No. 108845.
(11) El-Hajj, C.; Kyriacou, P. A. A Review of Machine Learning Techniques in Photoplethysmography for the Non-Invasive Cuff-Less Measurement of Blood Pressure. *Biomed Signal Process Control* **2020**, *58*, No. 101870.
(12) Lubin, M.; Vray, D.; Bonnet, S. Blood Pressure Measurement by Coupling an External Pressure and Photo-Plethysmographic Signals. *IEEE Eng. Med. Biol. Soc., EMBS* **2020**, 4996−4999.
(13) Le, T.; Ellington, F.; Lee, T. Y.; Vo, K.; Khine, M.; Krishnan, S. K.; Dutt, N.; Cao, H. Continuous Non-Invasive Blood Pressure Monitoring: A Methodological Review on Measurement Techniques. *IEEE Access* **2020**, *8*, 212478−212498.
(14) Perloff, D.; Grim, C.; Flack, J.; Frohlich, E. D.; Hill, M.; McDonald, M.; Morgenstern, B. Z. Human Blood Pressure: Determination by Sphygmomanometry. *Circulation* **1993**, *88* (5), 2460−2470.
(15) Nitzan, M. Automatic Noninvasive Measurement of Arterial Blood Pressure. *IEEE Instrum Meas Mag* **2011**, *14* (1), 32−37.
(16) Van Moer, W.; Lauwers, L.; Schoors, D.; Barbè, K. Linearizing Oscillometric Blood-Pressure Measurements: (Non)Sense? *IEEE Trans Instrum Meas* **2011**, *60* (4), 1267−1275.
(17) Bogatu, L. I.; Turco, S.; Mischi, M.; Muehlsteff, J.; Woerlee, P.An Experimental Study on the Blood Pressure Cuff as a Transducer for Oscillometric Blood Pressure Measurements. *IEEE Trans Instrum Meas.* **2021**, *70*, 1.
(18) Ramsey, M. Noninvasive Automatic Determination of Mean Arterial Pressure. *Med. Biol. Eng. Comput.* **1979**, *17* (1), 11−18.
(19) Kumar, S.; Yadav, S.; Kumar, A. Oscillometric Waveform Evaluation for Blood Pressure Devices. *Biomedical Engineering Advances* **2022**, *4*, No. 100046.
(20) Moraes, J. C. T. B.; Cerulli, M.; Ng, P. S. Development of a New Oscillometric Blood Pressure Measurement System. *Comput. Cardiol.* **1999**, 467−470.
(21) Drzewiecki, G.; Hood, R.; Apple, H. Theory of the Oscillometric Maximum and the Systolic and Diastolic Detection Ratios. *Ann. Biomed. Eng.* **1994**, *22* (1), 88−96.
(22) Asghar, W.; Li, F.; Zhou, Y.; Wu, Y.; Yu, Z.; Li, S.; Tang, D.; Han, X.; Shang, J.; Liu, Y.; Li, R. W. Piezocapacitive Flexible E-Skin Pressure Sensors Having Magnetically Grown Microstructures. *Adv. Mater. Technol.* **2020**, *5* (2), 1900934.
(23) Zhang, S.; Wang, C.; Ding, L.; Zhang, L.; Chen, J.; Huang, H.; Jiang, D.; Chen, Z.; Pan, G. A Flexible Bifunctional Sensor Based on Porous Copper Nanowire@ IonGel Composite Films for High-Resolution Stress/Deformation Detection. *J. Mater. Chem. C* **2020**, *8*, 4081−4092.
(24) Zang, Y.; Zhang, F.; Di, C. A.; Zhu, D. Advances of Flexible Pressure Sensors toward Artificial Intelligence and Health Care Applications. *Mater. Horiz* **2015**, *2* (2), 140−156.
(25) Lee, Y.; Park, J.; Cho, S.; Shin, Y. E.; Lee, H.; Kim, J.; Myoung, J.; Cho, S.; Kang, S.; Baig, C.; Ko, H. Flexible Ferroelectric Sensors with Ultrahigh Pressure Sensitivity and Linear Response over Exceptionally Broad Pressure Range. *ACS Nano* **2018**, *12* (4), 4045−4054.
(26) Shi, J.; Wang, L.; Dai, Z.; Zhao, L.; Du, M.; Li, H.; Fang, Y. Multiscale Hierarchical Design of a Flexible Piezoresistive Pressure Sensor with High Sensitivity and Wide Linearity Range. *Small* **2018**, *14* (27), 1800819.
(27) Xia, K.; Wang, C.; Jian, M.; Wang, Q.; Zhang, Y. CVD Growth of Fingerprint-like Patterned 3D Graphene Film for an Ultrasensitive Pressure Sensor. *Nano Res.* **2018**, *11* (2), 1124−1134.
(28) Xiong, Y.; Shen, Y.; Tian, L.; Hu, Y.; Zhu, P.; Sun, R.; Wong, C. P. A Flexible, Ultra-Highly Sensitive and Stable Capacitive Pressure Sensor with Convex Microarrays for Motion and Health Monitoring. *Nano Energy* **2020**, *70*, No. 104436.
(29) Li, H. Y.; Lee, C. S.; Kim, D. H.; Lee, J. H. Flexible Room-Temperature NH3 Sensor for Ultrasensitive, Selective, and Humidity-Independent Gas Detection. *ACS Appl. Mater. Interfaces* **2018**, *10* (33), 27858−27867.
(30) Wang, Z.; Zhang, L.; Liu, J.; Jiang, H.; Li, C. Flexible Hemispheric Microarrays of Highly Pressure-Sensitive Sensors Based on Breath Figure Method. *Nanoscale* **2018**, *10* (22), 10691−10698.
(31) Li, J.; Bao, R.; Tao, J.; Peng, Y.; Pan, C. Recent Progress in Flexible Pressure Sensor Arrays: From Design to Applications. *J. Mater. Chem. C Mater.* **2018**, *6* (44), 11878−11892.
(32) Meng, L.; Turner, A. P. F.; Mak, W. C. Soft and Flexible Material-Based Affinity Sensors. *Biotechnol Adv.* **2020**, *39*, 107398.
(33) Bijender; Kumar, A. Broadening the Utilization of Flexible and Wearable Pressure Sensors for the Monitoring of Health and Physiological Activities. *Biomed. Mater. Devices* **2023**, 1−13.
(34) Bijender; Kumar, A. Recent Progress in the Fabrication and Applications of Flexible Capacitive and Resistive Pressure Sensors. *Sens Actuators A Phys.* **2022**, *344*, No. 113770.
(35) Ding, Y.; Yang, J.; Tolle, C. R.; Zhu, Z. Flexible and Compressible PEDOT:PSS@Melamine Conductive Sponge Prepared via One-Step Dip Coating as Piezoresistive Pressure Sensor for Human Motion Detection. *ACS Appl. Mater. Interfaces* **2018**, *10* (18), 16077−16086.
(36) Bijender; Kumar, S.; Soni, A.; Kumar, A. Evaluation of Blood Pressure Using a Flexible and Wearable Capacitive Pressure Sensor. *RSC Adv.* **2023**, *13* (50), 35397−35407.
(37) Kumar, S.; Bijender; Yadav, S.; Kumar, A. Flexible Micro-hyperboloids Facets Giant Sensitive Ultra-Low Pressure Sensor. *Sens Actuators A Phys.* **2021**, *328*, No. 112767.
(38) Bijender; Kumar, A. Flexible and Wearable Capacitive Pressure Sensor for Blood Pressure Monitoring. *Sens Biosensing Res.* **2021**, *33*, No. 100434.
(39) Bijender; Kumar, A. One-Rupee Ultrasensitive Wearable Flexible Low-Pressure Sensor. *ACS Omega* **2020**, *5* (27), 16944−16950.
(40) Yang, J. C.; Kim, J. O.; Oh, J.; Kwon, S. Y.; Sim, J. Y.; Kim, D. W.; Choi, H. B.; Park, S. Microstructured Porous Pyramid-Based Ultrahigh Sensitive Pressure Sensor Insensitive to Strain and Temperature. *ACS Appl. Mater. Interfaces* **2019**, *11* (21), 19472−19480.
(41) Kumar, A. Effect of Porosity and Microstructure on the Functionality of Capacitive Pressure Sensors. *Mater. Chem. Phys.* **2023**, *304*, No. 127872.
(42) Ding, Y.; Xu, T.; Onyilagha, O.; Fong, H.; Zhu, Z. Recent Advances in Flexible and Wearable Pressure Sensors Based on Piezoresistive 3D Monolithic Conductive Sponges. *ACS Appl. Mater. Interfaces* **2019**, *11* (7), 6685−6704.
(43) Bae, J.; Hwang, Y.; Park, S. J.; Ha, J. H.; Kim, H. J.; Jang, A.; An, J.; Lee, C. S.; Park, S. H. Study on the Sensing Signal Profiles for Determination of Process Window of Flexible Sensors Based on Surface Treated PDMS/CNT Composite Patches. *Polymers* **2018**, *10* (9), 951.
(44) Choong, C. L.; Shim, M. B.; Lee, B. S.; Jeon, S.; Ko, D. S.; Kang, T. H.; Bae, J.; Lee, S. H.; Byun, K. E.; Im, J.; Jeong, Y. J.; Park, C. E.; Park, J. J.; Chung, U. I. Highly Stretchable Resistive Pressure Sensors Using a Conductive Elastomeric Composite on a Micropyramid Array. *Adv. Mater.* **2014**, *26* (21), 3451−3458.
(45) Pang, Y.; Zhang, K.; Yang, Z.; Jiang, S.; Ju, Z.; Li, Y.; Wang, X.; Wang, D.; Jian, M.; Zhang, Y.; Liang, R.; Tian, H.; Yang, Y.; Ren, T. L. Epidermis Microstructure Inspired Graphene Pressure Sensor with Random Distributed Spinosum for High Sensitivity and Large Linearity. *ACS Nano* **2018**, *12* (3), 2346−2354.
(46) Pang, Y.; Tian, H.; Tao, L.; Li, Y.; Wang, X.; Deng, N.; Yang, Y.; Ren, T. L. Flexible, Highly Sensitive, and Wearable Pressure and Strain Sensors with Graphene Porous Network Structure. *ACS Appl. Mater. Interfaces* **2016**, *8* (40), 26458−26462.
(47) Li, H.; Wu, K.; Xu, Z.; Wang, Z.; Meng, Y.; Li, L. Ultrahigh-Sensitivity Piezoresistive Pressure Sensors for Detection of Tiny Pressure. *ACS Appl. Mater. Interfaces* **2018**, *10* (24), 20826−20834.
(48) Wang, W.; Zheng, Y.; Jin, X.; Sun, Y.; Lu, B.; Wang, H.; Fang, J.; Shao, H.; Lin, T. Unexpectedly High Piezoelectricity of

https://doi.org/10.1021/acsomega.3c04786
ACS Omega 2024, 9, 6355−6365

Electrospun Polyacrylonitrile Nanofiber Membranes. *Nano Energy* **2019**, *56*, 588−594.
(49) Zhou, J.; Gu, Y.; Lu, J.; Xu, L.; Zhang, J.; Wang, D.; Wang, W. An Ultra-Strong Non-Pre-Irradiation and Self-Recoverable Mechano-luminescent Elastomer. *Chemical Engineering Journal* **2020**, *390*, No. 124473.
(50) Thakur, V. N.; Han, J. I. Combined Triboelectric and Piezoelectric Effect in ZnO/PVDF Hybrid-Based Fiber-Structured Nanogenerator with PDMS:Carbon Black Electrodes. *Polymers* **2022**, *14* (20), 4414.
(51) Thakur, V. N.; Han, J. I. Triboelectric Nanogenerator for Smart Traffic Monitoring and Safety. *J. Ind. Eng. Chem.* **2023**, *124*, 89−101, DOI: 10.1016/j.jiec.2023.04.028.
(52) Hsiao, V. K. S.; Leung, S. F.; Hsiao, Y. C.; Kung, P. K.; Lai, Y. C.; Lin, Z. H.; Salama, K. N.; Alshareef, H. N.; Wang, Z. L.; He, J. H. Photo-Carrier Extraction by Triboelectricity for Carrier Transport Layer-Free Photodetectors. *Nano Energy* **2019**, *65*, No. 103958.
(53) Zhong, T.; Zhang, M.; Fu, Y.; Han, Y.; Guan, H.; He, H.; Zhao, T.; Xing, L.; Xue, X.; Zhang, Y.; Zhan, Y. An Artificial Tribo-electricity-Brain-Behavior Closed Loop for Intelligent Olfactory Substitution. *Nano Energy* **2019**, *63*, No. 103884.
(54) Zhang, F.; Yang, K.; Pei, Z.; Wu, Y.; Sang, S.; Zhang, Q.; Jiao, H. A Highly Accurate Flexible Sensor System for Human Blood Pressure and Heart Rate Monitoring Based on Graphene/Sponge. *RSC Adv.* **2022**, *12* (4), 2391−2398.
(55) Yang, Y. F.; Yang, H.; Shang, J. C.; Zhao, W. H.; Yan, X.; Wan, Z. S.; Lei, H. S.; Chen, H. S. A High-Sensitivity Flexible PDMS@ rGO-Based Pressure Sensor with Ultra-Wide Working Range Based on Bioinspired Gradient Hierarchical Structure with Coplanar Electrodes. *Compos. Sci. Technol.* **2023**, *240*, No. 110078.
(56) Yun, Y. J.; Ju, J.; Lee, J. H.; Moon, S. H.; Park, S. J.; Kim, Y. H.; Hong, W. G.; Ha, D. H.; Jang, H.; Lee, G. H.; Chung, H. M.; Choi, J.; Nam, S. W.; Lee, S. H.; Jun, Y. Highly Elastic Graphene-Based Electronics Toward Electronic Skin. *Adv. Funct Mater.* **2017**, *27* (33), 1701513.
(57) Wang, D.-S.; Mukhtar, A.; Wu, K.-M.; Gu, L.; Cao, X. Multi-Segmented Nanowires: A High Tech Bright Future. *Materials* **2019**, *12* (23), 3908.
(58) Wang, D.; Mukhtar, A.; Humayun, M.; Wu, K.; Du, Z.; Wang, S.; Zhang, Y. A Critical Review on Nanowire-Motors: Design, Mechanism and Applications. *Chem. Rec.* **2022**, *22* (8), No. e202200016.
(59) Paghi, A.; Corsi, M.; Corso, S.; Mariani, S.; Barillaro, G. In Situ Controlled and Conformal Coating of Polydimethylsiloxane Foams with Silver Nanoparticle Networks with Tunable Piezo-Resistive Properties. *Nanoscale Horiz* **2022**, *7* (4), 425−436.
(60) Iglio, R.; Mariani, S.; Robbiano, V.; Strambini, L.; Barillaro, G. Flexible PDMS Foams Decorated with Multi−Walled CNTs for Unprecedented Detection of Ultralow Strain and Pressure Coupled with Large Working Range. *Electrochem. Soc. Meet. Abstr.* **2019**, 748.
(61) Heikenfeld, J.; Jajack, A.; Rogers, J.; Gutruf, P.; Tian, L.; Pan, T.; Li, R.; Khine, M.; Kim, J.; Wang, J.; Kim, J. Wearable Sensors: Modalities, Challenges, and Prospects. *Lab Chip* **2018**, *18* (2), 217−248.
(62) Meng, K.; Chen, J.; Li, X.; Wu, Y.; Fan, W.; Zhou, Z.; He, Q.; Wang, X.; Fan, X.; Zhang, Y.; Yang, J.; Wang, Z. L. Flexible Weaving Constructed Self-Powered Pressure Sensor Enabling Continuous Diagnosis of Cardiovascular Disease and Measurement of Cuffless Blood Pressure. *Adv. Funct Mater.* **2019**, *29* (5), 1806388.
(63) Luo, N.; Dai, W.; Li, C.; Zhou, Z.; Lu, L.; Poon, C. C. Y.; Chen, S. C.; Zhang, Y.; Zhao, N. Flexible Piezoresistive Sensor Patch Enabling Ultralow Power Cuffless Blood Pressure Measurement. *Adv. Funct Mater.* **2016**, *26* (8), 1178−1187.
(64) Wang, C.; Xia, K.; Wang, H.; Liang, X.; Yin, Z.; Zhang, Y. Advanced Carbon for Flexible and Wearable Electronics. *Adv. Mater.* **2019**, *31* (9), 1801072.
(65) Chen, W.; Yan, X. Progress in Achieving High-Performance Piezoresistive and Capacitive Flexible Pressure Sensors: A Review. *J. Mater. Sci. Technol.* **2020**, *43*, 175−188.
(66) Hou, C.; Wang, H.; Zhang, Q.; Li, Y.; Zhu, M. Highly Conductive, Flexible, and Compressible All-Graphene Passive Electronic Skin for Sensing Human Touch. *Adv. Mater.* **2014**, *26* (29), 5018−5024.
(67) Chen, S.; Jiang, K.; Lou, Z.; Chen, D.; Shen, G. Recent Developments in Graphene-Based Tactile Sensors and E-Skins. *Adv. Mater. Technol.* **2018**, *3* (2), 1700248.
(68) Wang, X.; Dong, L.; Zhang, H.; Yu, R.; Pan, C.; Wang, Z. L. Recent Progress in Electronic Skin. *Adv. Sci.* **2015**, *2* (10), 1500169.
(69) González-Rivera, J.; Iglio, R.; Barillaro, G.; Duce, C.; Tinè, M. R. Structural and Thermoanalytical Characterization of 3D Porous PDMS Foam Materials: The Effect of Impurities Derived from a Sugar Templating Process. *Polymers* **2018**, *10* (6), 616.
(70) Iglio, R.; Mariani, S.; Robbiano, V.; Strambini, L.; Barillaro, G. Flexible Polydimethylsiloxane Foams Decorated with Multiwalled Carbon Nanotubes Enable Unprecedented Detection of Ultralow Strain and Pressure Coupled with a Large Working Range. *ACS Appl. Mater. Interfaces* **2018**, *10* (16), 13877−13885.
(71) Stergiou, G. S.; Palatini, P.; Asmar, R.; Ioannidis, J. P.; Kollias, A.; Lacy, P.; McManus, R. J.; Myers, M. G.; Parati, G.; Shennan, A.; Wang, J.; O'Brien, E. Recommendations and Practical Guidance for Performing and Reporting Validation Studies According to the Universal Standard for the Validation of Blood Pressuremeasuring Devices by TheAssociation for the Advancement OfMedical Instrumentation/European Society OfHypertension/InternationalOrganization for Standardization (AAMI/ESH/ISO). *J. Hypertens* **2019**, *37* (3), 459−466.
(72) Chen, J.; Yao, B.; Li, C.; Shi, G. An Improved Hummers Method for Eco-Friendly Synthesis of Graphene Oxide. *Carbon N Y* **2013**, *64*, 225−229.
(73) Surekha, G.; Krishnaiah, K. V.; Ravi, N.; Padma Suvarna, R. FTIR, Raman and XRD Analysis of Graphene Oxide Films Prepared by Modified Hummers Method. *J. Phys. Conf Ser.* **2020**, *1495* (1), No. 012012.
(74) Celler, B. G.; Argha, A.; Le, P. N.; Ambikairajah, E. Novel Methods of Testing and Calibration of Oscillometric Blood Pressure Monitors. *PLoS One* **2018**, *13* (8), No. e0201123.
(75) Uuiversitc Canadienne Canada's University, L.; Chen, S.; Bolic, M.*Improving Algorithms for Oscillometric Blood Pressure Estimation by Suppressing Breathing Effects*. 2010. DOI: 10.20381/RUOR-137.
(76) Giavarina, D. Understanding Bland Altman Analysis. *Biochem Med. (Zagreb)* **2015**, *25* (2), 141−151.

https://doi.org/10.1021/acsomega.3c04786
ACS Omega 2024, 9, 6355−6365